University of Kent

Kent Academic Repository

Stancu, Radu-Florin, Hughes, Michael, Marques, Manuel J., Seneci, Carlo, Henry, Ross, Ourselin, Sébastien, da Cruz, Lyndon, Bergeles, Christos and Podoleanu, Adrian G.H. (2026) *Ultra-thin, forward-viewing OCT endoscope using a rotating angle-cleaved fiber*. Biomedical Optics Express, 17 (11). pp. 5920-5931. ISSN 2156-7085.

Downloaded from

https://kar.kent.ac.uk/117316/ The University of Kent's Academic Repository KAR

The version of record is available from

https://doi.org/10.1364/BOE.614912

This document version

Publisher pdf

DOI for this version

Licence for this version

CC BY (Attribution)

Additional information

Versions of research works

Versions of Record

If this version is the version of record, it is the same as the published version available on the publisher's web site. Cite as the published version.

Author Accepted Manuscripts

If this document is identified as the Author Accepted Manuscript it is the version after peer review but before type setting, copy editing or publisher branding. Cite as Surname, Initial. (Year) 'Title of article'. To be published in ***Title of Journal*** , Volume and issue numbers [peer-reviewed accepted version]. Available at: DOI or URL (Accessed: date).

Enquiries

If you have questions about this document contact ResearchSupport@kent.ac.uk. Please include the URL of the record in KAR. If you believe that your, or a third party's rights have been compromised through this document please see our Take Down policy (available from https://www.kent.ac.uk/guides/kar-the-kent-academic-repository#policies).

Research Article Vol. 17, No. 11 / 1 Nov 2026 / Biomedical Optics Express 5920
Biomedical Optics EXPRESS

Ultra-thin, forward-viewing OCT endoscope using a rotating angle-cleaved fiber

RADU-FLORIN STANCU,[1,*,†] MICHAEL HUGHES,[1,†] MANUEL J. MARQUES,[1,†] CARLO SENECI,[2] ROSS HENRY,[2,3] SÉBASTIEN OURSELIN,[2] LYNDON DA CRUZ,[3] CHRISTOS BERGELES,[2] AND ADRIAN PODOLEANU[1]

[1] *University of Kent, Applied Optics Group, School of Engineering, Mathematics and Physics, Canterbury, CT2 7NH, UK*
[2] *King's College London, Robotics and Vision in Medicine Lab, School of Biomedical Engineering & Imaging Sciences, 1 Lambeth Palace Rd, South Bank, London, SE1 7EU, UK*
[3] *Moorfields Eye Hospital, 162 City Road, London, EC1 V 2PD, UK*
[†] These authors contributed equally.
[*] *r.stancu@kent.ac.uk*

Abstract: While ultra-thin optical coherence tomography (OCT) probes using rotating fibers have been demonstrated in side-viewing configurations, achieving fully miniaturized forward-viewing OCT endoscopy remains challenging because of the need to incorporate a lateral scanning mechanism. Here, we report a forward-viewing OCT fiber endoscope that can fit inside a protective tube with an inner diameter of 0.16 mm, enabling an endoscope with an outer diameter of 0.31 mm. The rotating fiber assembly incorporates a gradient-index fiber lens and an angle-cleaved length of no-core fiber at the distal tip. This causes the beam to exit at an angle to the endoscope axis, such that rotating the fiber using an external rotary coupler generates circular scanning of the beam over the tissue. Lateral and axial resolutions of 25 µm and 11 µm, respectively, are achieved at focus, with a usable imaging depth range of over 2 mm and an image circle circumference of 950 µm at 1 mm from the fiber tip. An exemplar application in vitreoretinal surgery is demonstrated by *ex vivo* porcine retinal imaging and real-time monitoring of a surgical tool interacting with the tissue.

Published by Optica Publishing Group under the terms of the Creative Commons Attribution 4.0 License. Further distribution of this work must maintain attribution to the author(s) and the published article's title, journal citation, and DOI.

1. Introduction

Optical coherence tomography (OCT) is an imaging technique that is widely used in ophthalmology and a range of other medical applications. It provides high-resolution cross-sectional and volumetric images, typically penetrating up to a millimeter into scattering tissue. Endoscopic, catheter, and needle probes extend OCT imaging to internal organs or deeper into scattering tissue [1]. Further reducing the size of OCT probes is of great interest for extending the range of applications and minimizing invasiveness but involves solving numerous challenges raised by the need to miniaturize the beam-scanning mechanism.

The thinnest OCT probes are currently side-viewing designs. An optical fiber is terminated with an approximately 45° angled cut [2], a tilted MEMS mirror [3], a prism [4], or another element that deflects the beam by approximately 90°, so that it exits to the side of the probe. Rotating the fiber within an outer housing, using a mechanism external to the patient, results in a circular scan, concentric with the fiber. Simultaneous translation of the probe along the axis generates a spiral scan and hence achieves volumetric imaging. OCT catheters and endoscopes are typically in the region of 3 mm outer diameter [5], but since a minimalist probe requires only

#614912 https://doi.org/10.1364/BOE.614912
Journal © 2026 Received 26 Aug 2026; revised 16 Oct 2026; accepted 16 Oct 2026; published 26 Oct 2026

Biomedical Optics EXPRESS

a fiber rotating within an outer sheath or needle, implementations as small as 0.46 mm [6] have been reported.

The side-viewing approach is well-optimized for imaging tubular structures [7], such as the gastrointestinal tract [8], pulmonary airways [9], or arteries [10]. Recent developments include a side-viewing endoscopic probe that combines OCT and angle-resolved low-coherence interferometry (a/LCI) [11], which enables more accurate detection of esophageal dysplasia. However, for applications such as retinal imaging during vitreoretinal surgery, a forward-viewing probe is required. Unfortunately, obtaining lateral scanning in forward-viewing probes is more challenging. High-speed scanning in one or two directions can be achieved by vibrating the tip of a fiber proximal to a lens, for example using a piezoelectric actuator [12]. Designs using 1-D fiber cantilever optical scanner, driven by an electrothermal MEMS actuator, have also been reported, but they exhibit, generally, a large diameter, such as 5.5 mm [13]. Approaches using fiber imaging bundles to avoid distal scanning entirely have been investigated but currently do not provide sufficient image quality for clinical use [14].

The smallest functional designs use proximally driven rotational motion, relying on a mechanism to convert rotational motion to forward-viewing circular or linear scanning at the distal tip. For example, a pair of rotating wedges (also known as a Risley prism pair) can work in concert to steer a beam in two dimensions. However, a reported implementation of this concept with a gradient-index (GRIN) lens and prism required an outer diameter of 2.5 mm [15]. Issues such as chromatic aberrations must also be managed [16]. A much smaller 21-gauge (0.82 mm diameter) needle probe used rotation of a pair of angled elements to achieve a linear scan in front of the probe [17], although this was limited to a frame rate of 0.5 Hz and is still large compared with ophthalmic catheters, which are typically 23-gauge [18], 25-gauge [19], or 27-gauge [20]. Another approach is to have a pre-bent fiber protruding outside of the probe; rotating the probe then sweeps a circular scan [21]. This achieved a reported probe diameter as small as 0.5 mm, but protecting the rotating tip from the environment requires a further outer sheath with a 0.7 mm diameter.

An alternative is to convert axial translation to lateral scanning by sliding a tube over a pre-bent 'S' shaped fiber, which has been shown to allow a 25-gauge (0.51 mm) outer diameter and frame rates of 5 Hz [22]. Needle probes using GRIN rod lenses as relays have also been demonstrated [23], but these are entirely rigid, requiring the scanning system to be placed close to the eye, and suffer from a small field-of-view.

Here, we focus on the design and experimental validation of an ultra-miniaturized forward-viewing OCT probe. It is particularly targeted towards vitreoretinal surgical procedures such as those described in Refs. [24–26], where the need for miniaturization is most extreme. These interventions demand extremely high precision, as surgeons need to manually manipulate delicate tissues with sub-millimeter accuracy, while ensuring patient safety. For this reason, there is growing interest in robot-assisted vitreoretinal surgery [27,28], especially as even more demanding sub- and intra-retinal therapy delivery interventions are considered.

Regardless of whether the surgery is manual or assisted, traditional visualization methods have limitations; surgical microscopes with white light illumination achieve high magnification but do not provide volumetric or sub-surface imaging. For this reason, OCT has already been widely used in retinal procedures [29], but almost always using external systems integrated within the surgical microscope. The image quality is therefore dependent on the clarity of the ocular media and an unobstructed field of view inside the eye. Furthermore, the introduction of opaque surgical tools into the field-of-view tends to block the beam, creating shadows on the OCT images. This issue could be mitigated if an imaging probe was integrated into the tools themselves, or into other instruments such as the light pipe used for illumination.

In this paper we describe a new approach to endoscopic OCT termed μFV-OCT (micro forward-viewing OCT). It makes use of a lensed optical fiber probe designed to cause the beam

Biomedical Optics EXPRESS

to exit at an angle to the optical axis. Rotation of the fiber therefore causes the beam to sweep out an arc in front of the probe. The rotation can be driven from the proximal end, well away from the tissue, while the probe itself is as thin as the fiber, with the final endoscope diameter being determined by that of the outer sheath within which the fiber rotates.

The fiber must have a lens at the distal tip to improve collection efficiency and maintain a reasonable working distance, and the lens diameter should not exceed the fiber diameter. There are several possible approaches to this, such as attaching a segment of no-core fiber (NCF) with a curved surface to act as a lens [30] or forming a ball lens at the tip [31]. In this work, we use segments of NCF and GRIN fiber, an approach previously shown to provide a good combination of resolution and working distances [32]. An additional segment of NCF fiber at the distal end allows an angled cleave to be made, with refraction at this surface leading to an angled beam, thus converting rotation of the fiber into circular scanning in a forward-viewing direction.

Below, we describe the fabrication and operation of the fiber probes in more detail and evaluate their optical performance with a swept-source OCT system. We demonstrate imaging of phantoms and *ex vivo* animal retinal tissue and show how the probes could be used to visualize a needle interacting with the tissue.

2. Methods

A schematic of the μFV-OCT imaging system is shown in Fig. 1. The OCT system employs a swept source with a 1060 nm central wavelength, 135 nm bandwidth, and 100 kHz sweeping rate (Axsun AXP50124-3). 20% of the light is sent to the fiber probe, while the remainder is used as the reference signal. The optical power on the sample is 1.08 mW.

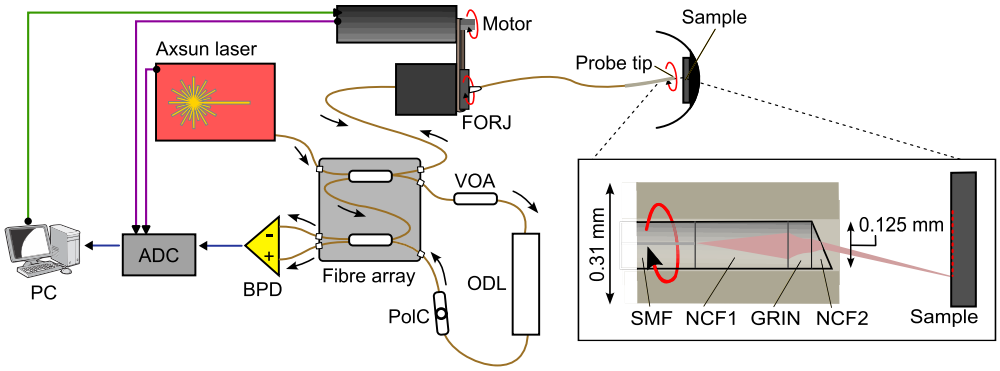


Fig. 1. Overview of μFV-OCT, showing an OCT interferometer and a fiber probe rotated by the motor and fiber optic rotating junction (FORJ). The inset shows a close-up view of the probe tip. VOA: variable optical attenuator, BPD: balanced photodetector, ADC: analog-to-digital converter, ODL: optical delay line, PolC: polarization controller, SMF: single-mode fiber, NCF1 and NCF2: no-core (no-core) fiber, GRIN: gradient-index fiber.

The reference arm of the interferometer includes a variable optical attenuator (VOA, AFW Technologies VOA-SM-64-L-1-2), which enables optical power management to avoid detector saturation, and a motorized optical delay line (ODL, Gooch & Housego SFF-ODL) with a maximum range of 160 mm, interfaced via a driver board (Trinamics TMCM-1140). The ODL allows rapid interchange of probes fabricated with slightly different lengths. The system employs balanced detection, with the signals from a 1 GHz balanced photodetector (BPD, Thorlabs PDB481C-AC) digitized by an analog-to-digital converter board (ADC, Acqiris SA220E).

The imaging probe fiber assemblies were fabricated using the thermal splicing function of a Vytran GPX-3400 glass-processing system and a high-precision LDC400 Vytran fiber cleaver.

Biomedical Optics EXPRESS

Full details of the method for splicing short lengths of GRIN and NCF are provided in Ref. [33]. The probe is mostly comprised of Hi1060 single-mode fiber (SMF), with the distal end including a beam-expanding 350 µm long section of no-core fiber (NCF1), a 70 µm long multimode GRIN fiber section acting as a focusing lens, and a short angled-cut NCF section (NCF2), which causes the beam to be deflected due to refraction. The design was modelled using the approach and code provided in Ref. [33], and these lengths were selected so as to provide a balance between working distance (predicted to be 820 µm), lateral spot size (predicted to be 13 µm), and light collection efficiency (which generally decreases with working distance). The working distance could be increased, if desired, at the expense of focused spot size.

The angle cleave of the probe tip is achieved by pre-twisting the fiber before cleaving. The beam exit angle, α, is related to the cleave angle, θ, by:

$$\alpha = \arcsin\left(\frac{n_{\text{NCF}}}{n_{\text{media}}}\sin\theta\right) - \theta,$$

where n_{NCF} is the refractive index of the no-core fiber and n_{media} is the refractive index of the medium beyond the angle cleave, normally expected to be air, i.e. $n_{\text{media}} = 1$.

The fiber is rotated inside an outer tube by a single-channel fiber-optic rotating junction (FORJ, Princetel MJP-SAPB) which allows continuous rotation of the OCT fiber probe without twisting. The probe is connected to the FORJ via an SC/APC connector for quick interchange. For validation purposes, the fiber probe is rotated inside an outer plastic tubing terminated with a 30-gauge needle with an inner diameter of 0.16 mm and an outer diameter of 0.31 mm.

The FORJ is driven by a 24 V brushless motor (Maxon ECXSP13M + GPX13SPHS + ENX13 EASYINTCOMM), via a 2 mm pitch timing belt (RS1430, Automotion Components) and aluminum pulley (zinc plated flanges, 6.4 mm belt width, 2 mm pitch, 44 teeth, RS Pro). The motor and FORJ are mounted inside a custom 3D-printed assembly, which also includes the timing belt tensioning mechanism. The motor is controlled through a Maxon EPOS4 positioning controller with an EPOS4 EtherCAT card. A synchronization pulse from the motor is used to trigger frame acquisition from the ADC board. For all images shown below, the fiber was rotated at 10 Hz, giving 10,000 spectra per rotation. This was down-sampled by averaging groups of 10 spectra to give 1,000 spectra per B-scan. Standard OCT image reconstruction procedures were applied to recover OCT B-scans, including k-space linearization by Kaiser-Bessel interpolation, intrinsic dispersion compensation, and background subtraction. All images displayed below are log-scaled.

As the probe rotates, a series of A-scans are collected, each beginning at the distal end of the fiber assembly, and together forming the surface of a cone, shown in Fig. 2(a). Raw B-scans can be displayed with rotation angle along the horizontal axis and axial position (i.e., the distance from the fiber tip) along the vertical axis, as in Fig. 2(b). Since the imaged area is the surface of a cone, this leads to distorted images, where the lateral scale varies along the depth direction, and the circular nature of the scan is obscured. This is illustrated by the colored scattering features from Fig. 2(a) appearing to vary in size with depth, z, in Fig. 2(b), where the lateral pixel size, Δx, is given by:

$$\Delta x(z) = 2\pi z \sin\alpha / N$$

where α is the angle of the beam exiting the fiber, relative to the fiber axis, and N is the number of A-scans making up the image.

The scans can be mapped to a polar scan, as is typically done for side-viewing OCT probes, and this is illustrated in Fig. 2(c). For a side-viewing probe, with the beam exiting at 90° to the axis of rotation, this would produce an undistorted image, but this is not the case for the cone-like scanning here. At a particular depth, z, the circular scan has a real physical circumference of:

$$c = 2\pi z \sin\alpha,$$

Biomedical Optics EXPRESS

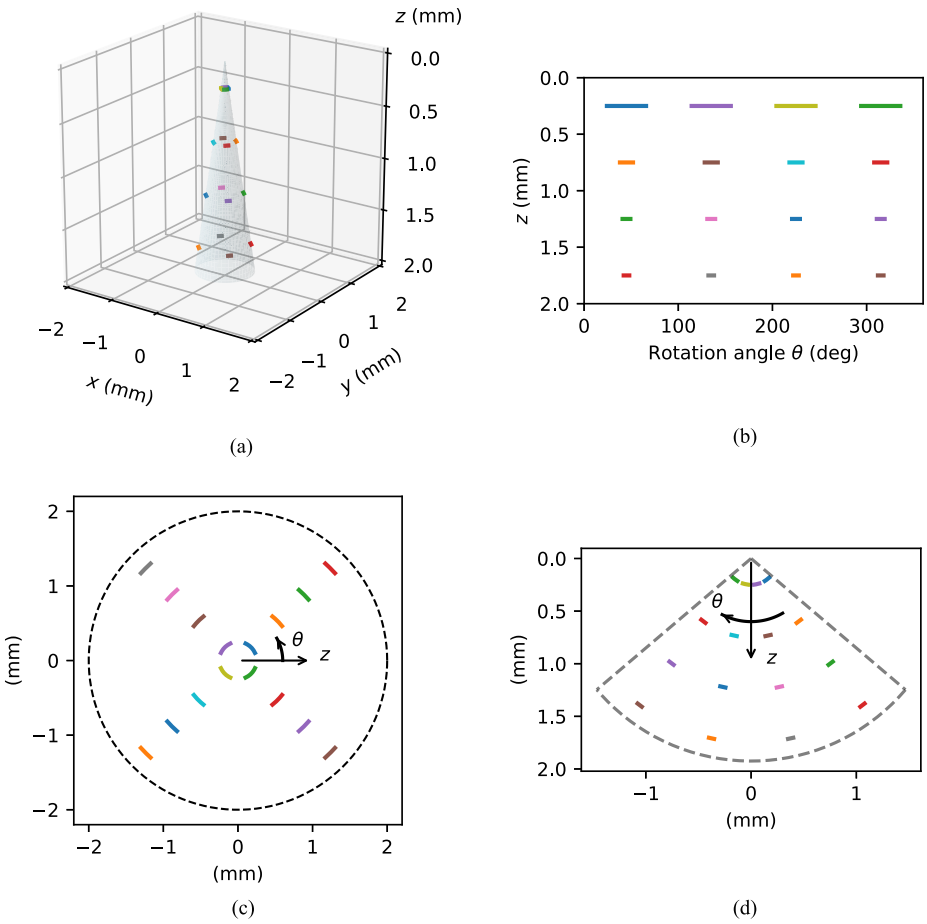


Fig. 2. Illustration of possible ways to display images. (a) Scanning cone, showing locations of example scattering objects that intersect the cone as colored marks. (b) Simple mapping of depth on the vertical axis and rotation angle along the horizontal axis, leading to obvious distortion of object sizes; the effective increase in pixel size with depth causes deeper objects to appear smaller. (c) Polar plot, maintaining constant size with depth but elongating features in the angular direction. (d) Sector plot, maintaining feature size but obscuring circular scan geometry.

while in the polar image the corresponding circle has a circumference of:

$$c' = 2\pi m z,$$

where m is the scaling between physical depth, z, and radial position in pixels in the image. Hence,

$$c' = mc/\sin\alpha.$$

For the radial image to have horizontal and vertical pixel sizes which are constant across the image, we require that the scaling of length along the scanning arc (i.e. along the angular direction) is equal to the scaling of lengths in the radial (depth) direction, i.e.:

$$c' = mc,$$

which clearly only holds for $\alpha = 90^0$, i.e. a conventional side-viewing probe. For the forward-viewing probes reported here, $\sin\alpha \approx 0.28$, and hence the radial scaling and angular scaling

Biomedical Optics EXPRESS

are substantially different. This tends to make the images appear distorted, with speckle grains elongated along the angular direction.

An alternative approach is to map the images to a sector of a circle such that the arc length and radial distances have the same scale, as shown in Fig. 2(d). This is achieved by mapping the probe rotational position θ to angle ϕ in the image:

$$\phi = \theta \sin\alpha$$

At depth z, the circle of real circumference $c = 2\pi z \sin\alpha$ is then mapped to an arc of length $c' = 2\pi \mathrm{mz}\ \sin\alpha$ which achieves $c' = mc$. However, this is at the cost of once again obscuring the circular nature of the scan, since the image is now not a complete circle, and it is not visually apparent that points on the two lateral extremes of an arc in the image correspond to neighboring points on the tissue. It should be noted that these remappings do not take account of refractive index changes within the tissue or between the medium and the tissue.

3. Results and discussion

Following fabrication, probes were inspected under the built-in microscope of the Vytran glass-processing system. The joints between the fiber sections were visible, allowing measurement of the achieved fiber lengths, which typically vary by up to 10 µm from the design length. Modelling using ABCD matrices, following the approach and code provided in Ref. [32], suggests that the performance of the probe is most sensitive to variations in the length of the GRIN segment, with a change of ±5 µm predicted to change the focal spot size by as much as 5 µm, and the distance of the focus from the tip by up to 200 µm. In comparison, changes in the lengths of the NCF segments by ±5 µm change the focal spot size by less than 1 µm and position by 20 µm. Given the low cost of materials, it is feasible to build several probes and select only those that perform within desired specifications.

An example of a microscope image is shown in Fig. 3 for a probe with a cleave angle of 18°. The optical loss due to the addition of the three fiber segments to the single-mode fiber was measured to be 4.2%.

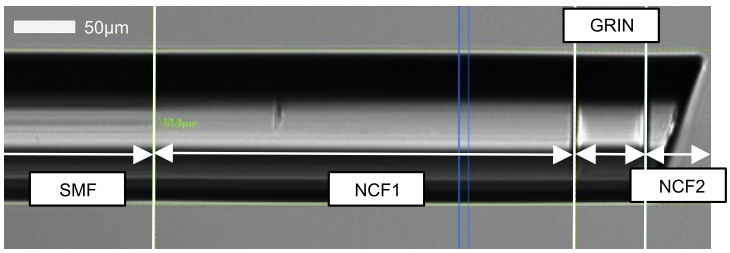


Fig. 3. Example of an image of the OCT probe angle cleaved at 18°, delivered by the Vytran microscope. The single-mode fiber (SMF), beam-expanding no-core fiber (NCF1), the focusing gradient-index fiber (GRIN), and the second no-core fiber (NCF2), which is angle-cleaved, are indicated. Scale bar is 50 µm.

The optical performance of the probes was evaluated by imaging the focused spot created by the lensed fiber onto a Thorlabs CP33TM camera via a 10X microscope objective. Figure 4(a) shows an example from a probe with an 18° angle cleave. As can be seen, the angle-cleaved fiber end results in an elongated focus. Despite this, it should be noted that the minor axis of the beam is aligned with the rotational scan direction, and so the apparent lateral resolution across the B-Scans is governed by the minor-axis FWHM rather than the mean. Plots are shown of the radially-averaged intensity in Fig. 4(b) and horizontal and vertical profiles through the spot in Fig. 4(c). Fitting a 2D Gaussian with rotational freedom gives a minor-axis full-width at

Biomedical Optics EXPRESS

half-maximum (FWHM) of 16.1 µm, a major-axis FWHM of 32.0 µm, a geometric mean FWHM of 22.7 µm, and an eccentricity of 0.85.

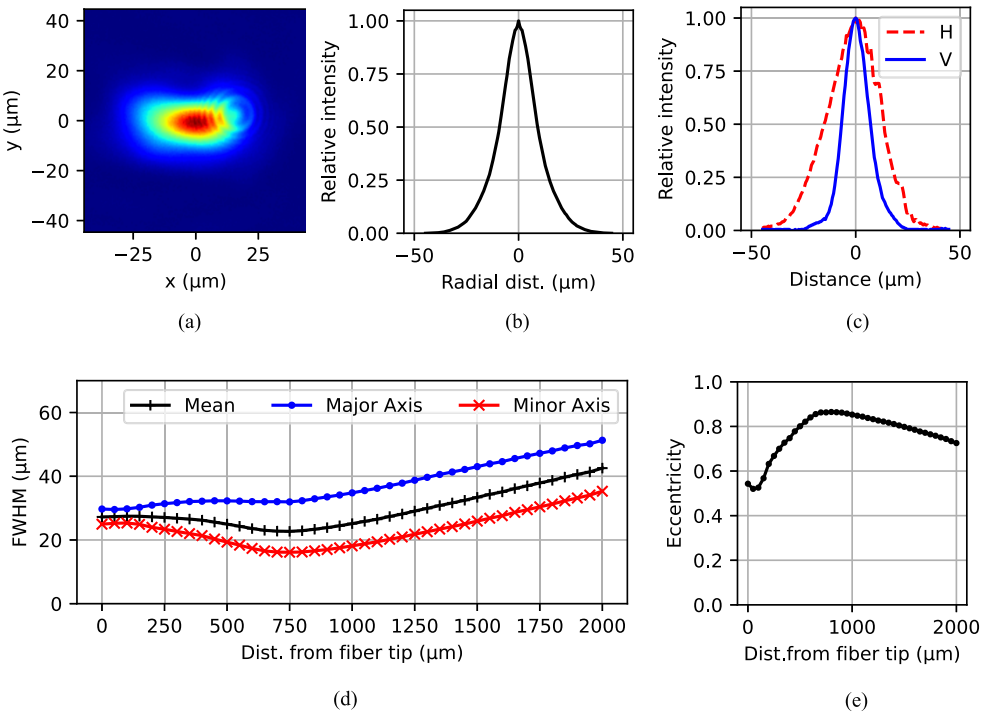


Fig. 4. Characterization of the focused spot generated from an angled fiber probe C (Table 1). (a) Focal spot from fiber with approximately 18° angle cleave (9.0° beam exit angle), showing elliptical shape. (b) Radially-averaged profile through (a). (c) Horizontal and vertical profiles through (a). (d) Geometric mean and minor and major axis FWHM of spot as a function of distance from fiber tip, obtained by fitting a 2D Gaussian function. (e) Eccentricity of spot as a function of distance from fiber tip.

Table 1. OCT probe parameters

Parameter	Probe A	Probe B	Probe C
Pre-cleave twist angle	40°	60°	90°
Cleave angle (measured)	9.7°	13.8°	18.0°
Cleave angle (theoretical)	7.7°	11.4°	18.5°
Beam angle (measured)	3.5°	5.3°	9.0°
NCF1 length	350.0 µm	347.9 µm	350.1 µm
GRIN length	70.3 µm	72.6 µm	71.1 µm
NCF2 length	28.9 µm	44.1 µm	64.3 µm
Total length	71.5 cm	65.0 cm	67.0 cm

Figure 4(d) shows how the spot FWHM changes as a function of distance from the fiber tip. Radially-averaged intensity, horizontal and vertical profiles register a minimum at a distance

Biomedical Optics EXPRESS

from the tip of the fiber of approximately 750 µm. This can be considered as the nominal working distance of the probe. The mean FWHM remains under 40 µm up to nearly 2 mm from the fiber tip. Eccentricity also varies with distance, with a maximum eccentricity close to the working distance, as shown in Fig. 4(e).

Three probes, A, B and C were fabricated, with parameters listed in Table 1, with pre-cleave twists of 40°, 60°, and 90°, resulting in cleave angles of approximately 9.7°, 13.8° and 18° as measured under a microscope. Other properties were designed to be identical, but the fabrication process has some inherent uncertainty, and so the measured parameters, including fiber lengths, cleave angles, spot minor and major axis lengths, spot eccentricities, and working distances are listed in Table 1. The beam exit angles were found to be 3.5°, 5.3°, and 9° which would be expected for cleave angles of 7.7°, 11.4°. and 18.5°. The small discrepancy from the measured cleave angles may arise from the difficulty of exactly measuring the angle under a microscope.

To confirm the beam exit angle, and hence the size of the scanned circle at a given distance from the fiber tip, a video was recorded during rotation of the fiber using the same microscope setup employed for measuring the spot FWHM. The location of the spot was identified as the peak intensity in each image, and a circle was fitted to these points. This was repeated at multiple distances from the fiber end. Figure 5(a) shows the circumference of the scanned circle as a function of distance from the fiber end, which, as expected, grows linearly with distance. From this data, the beam angle was measured to be 9.0°. This is the expected beam angle from a cleave angle of 18.5°, similar to the measured cleave angle of 18°. The red dashed line shows the number of resolution elements in the scanned line at each distance, i.e., the length of the line divided by the spot minor-axis FWHM at each distance. From a distance of 800 µm onwards, there are at least 50 resolution elements spanning the circumference of the circle.

The sensitivity of the probe as a function of working distance was determined by collecting scans of a sheet of paper, moved in 100 µm steps away from the tip of the fiber. The resulting OCT signal, averaged over a depth range of 70 µm beneath the paper surface, is shown against the distance from the probe tip in Fig. 5(b). Note that, while sensitivity roll-off from the OCT interferometer is present, it is negligible over 2 mm due to the long coherence length of the source. The decay in signal with distance of approximately 6 dB per 0.5 mm is therefore primarily due to the depth-of-field of the fiber probe.

The absolute sensitivity was measured to be 89 dB at a working distance of 250 µm for approximately 1 mW optical power to the sample. This was determined by aligning a mirror in front of the probe to maximize the returned power to the detector, measured using an optical power meter, misaligning the mirror to reduce the power by a factor of 1000, acquiring an OCT image, measuring the signal-to-noise ratio, and combining with the known attenuation. This measurement was made using the same factor of 10 A-scan averaging as later used for imaging (i.e. with an effective A-scan rate of 10 kHz). This may be an under-estimate of the true sensitivity due to the difficulties of precisely aligning a tilted mirror at such a short distance from the probe tip. Additionally, a spurious loss of 4 dB was measured in the rotating coupler; if this was reduced to a typical best-case 0.5 dB, the shot-noise limited sensitivity would theoretically increase to 92.5 dB for the same power on the sample.

Reducing the angle of the cleave, and hence the beam exit angle, decreases the eccentricity of the focused spot and decreases the lateral spot FWHM. However, this also decreases the size of the scanned circle at a given distance in proportion to the reduced beam exit angle.

Examples of the focused beam at the working distance from fiber probe A (beam exit angle of 3.5°) and fiber probe B (beam exit angle of 5.3°) are shown in Fig. 5(c) and Fig. 5(d), respectively. Radially-averaged profiles through both are shown in Fig. 5(e) and are compared with the profile from fiber probe C with an 18° angle cleave (beam exit angle of 9.0°), as characterized previously. The eccentricities of the spot at focus for the 3.5° and 5.3° beam angle probes are 0.74 and 0.77, while the mean FWHMs are 12.7 µm and 16.3 µm, respectively. There is therefore a penalty for

Biomedical Optics EXPRESS

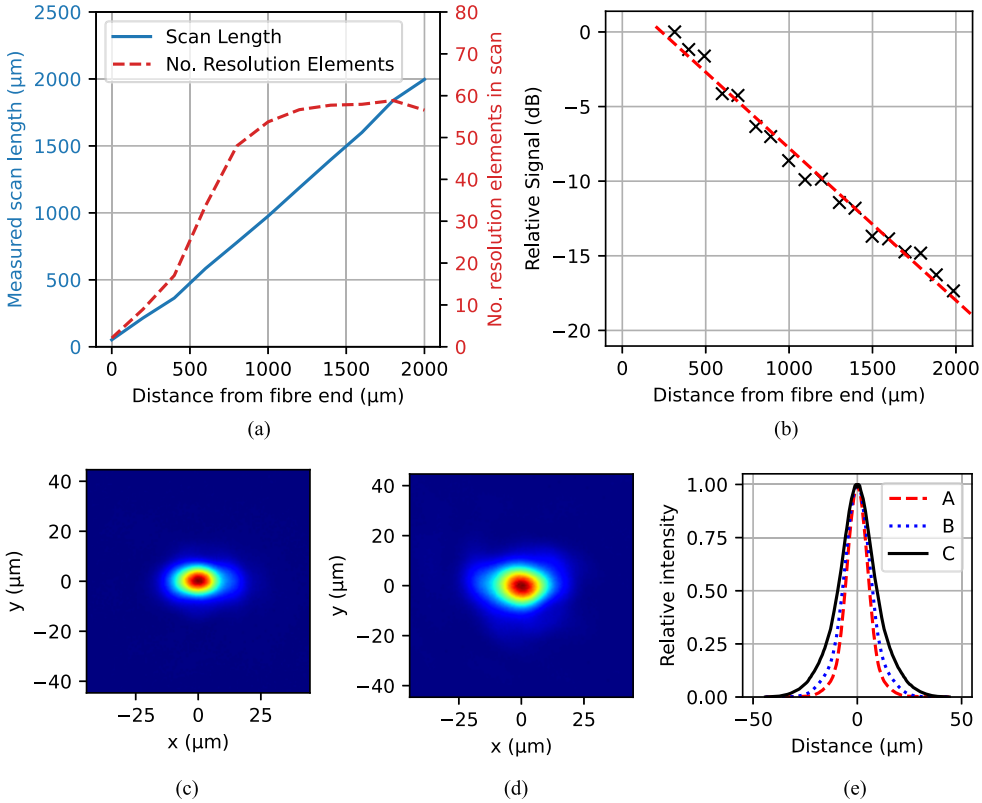


Fig. 5. (a) Scan circle length (blue, solid) as a function of distance from the end of rotating fiber probe C characterized in Fig. 4, with a beam exit angle of 9.0° (due to a cleave angle of approximately 18°). The red dashed line shows the number of resolution elements along the line at each distance, obtained by dividing the line length at that distance by the corresponding spot FWHM. (b) Relative sensitivity as a function of distance from the fiber tip for probe C. (c) Focused spot from fiber probe A with 3.5° beam exit angle. (d) Focused spot from fiber probe B with 5.3° beam exit angle. (e) Radial plots through focused spots from fiber probes A, B, and C.

increased beam angle (and increased image scanning size) in terms of decreased lateral resolution. All subsequent results are from Probe C.

The axial resolution (FWHM) was determined as (11.7 ± 0.7) µm in air by fitting a Gaussian to an A-scan of a mirror and does not depend on the specific design of the probe.

To validate tissue imaging, B-scans were recorded from *ex vivo* porcine retina at a frame rate of 10 Hz, as shown in Fig. 6. Figure 6(a) shows the raw B-scan, with scan angle along the horizontal direction and distance from the fiber tip along the vertical direction. Figure 6(b) shows the same data mapped to a polar plot, and Fig. 6(c) shows it mapped to a sector plot. Figure 6(d-g) shows the same tissue at different axial distances from the probe. Due to the cone-shaped scan, changing the axial distance also changed the lateral position of the sample that is imaged.

A potential application of the probe is to monitor tool-tissue interactions during retinal surgery. To demonstrate the feasibility of this, a 30-gauge needle (0.31 mm outer diameter) was imaged together with *ex vivo* retinal tissue, as shown in Fig. 7(a-d). The needle was introduced at approximately 45° to the tissue and at 90° to the imaging probe. The surface of the needle is visible as a bright reflection, indicated in the figure with an asterisk (*). In Fig. 7(a), the needle

Biomedical Optics EXPRESS

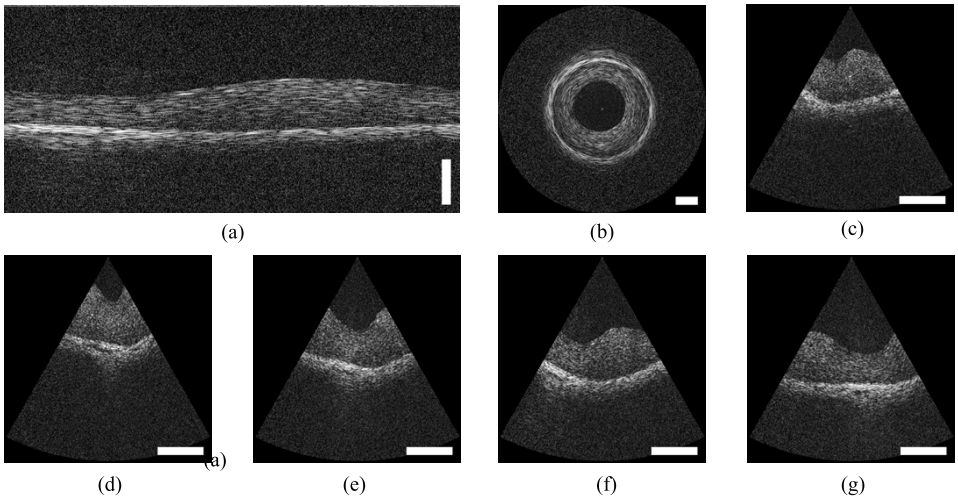


Fig. 6. Imaging results from porcine retina *ex vivo*, imaged in air: (a) raw B-scan, with depth along the vertical and angle along the horizontal; (b) the same data as in (a) but in a radial plot; (c) the same data again in a segment plot; (d-g) examples of the same retina with the probe moved (d) -100 µm (e) + 100 µm, (f) + 200 µm and (g) + 300 µm relative to the data in (a-c). Note that the lateral position of the scan also changes as the distance changes. The scale bars are 0.5 mm in air, but for (a) the scale bar is only valid in the vertical direction and for (b) in the radial direction. For (c-g) the scale bar is valid in both directions.

is just touching the top of the tissue, while in Fig. 7(b) and Fig. 7(c) the needle has penetrated inside. Figure 7(d) shows an example of the needle just above the tissue and close to the probe, causing it to cast large shadows which obscure most of the tissue. Note that the signal from the needle does not necessarily indicate the location of its tip; the reflection occurs at the point the needle intersects the scanning cone.

For *in vivo i*maging applications, where the probe may be submersed in liquid such as the vitreous humor of the eye, it would be necessary to seal the end of the outer tube with a transparent window, both to prevent fouling of the probe and to preserve the angular deflection which relies on refraction. To demonstrate feasibility of imaging when the probe is immersed in liquid and through a window, a 0.13-0.17 mm thick glass coverslip was placed at the end of the outer tube. The focal spot was measured using the same method as above, and it was confirmed that the introduction of the coverslip makes no significant difference to the FWHM of the spot at focus (a change of < 0.2 µm, which is within likely experimental error).

A piece of laminated paper was imaged, first without the window, Fig. 7(e), then through the window, Fig. 7(f), and finally through the window with water introduced between the paper and the window, Fig. 7(g). The images all appear qualitatively similar. Figure 7(h) shows *ex vivo* retinal tissue imaged through the window, with water between the retina and the window. The delicate *ex vivo* retinal surface may have been degraded by the presence of the water, and so the image is not directly comparable to images of the retina in air. Nevertheless, the results demonstrate that good imaging can be achieved through a window.

If the 0.31 mm sealed probe would be integrated in an intraocular vitreoretinal surgical procedure, a fully miniaturized transparent window would be required for patient safety, preventing direct contact between the fiber probe itself and the retinal surface. The window would need to be water-tight, and the entire assembly suitable to be sterilized. The optical properties of a fully-miniaturized window are expected to be similar to the glass coverslip that was evaluated here, and so no additional degradation of image quality is expected. Neither would the introduction of

Biomedical Optics EXPRESS

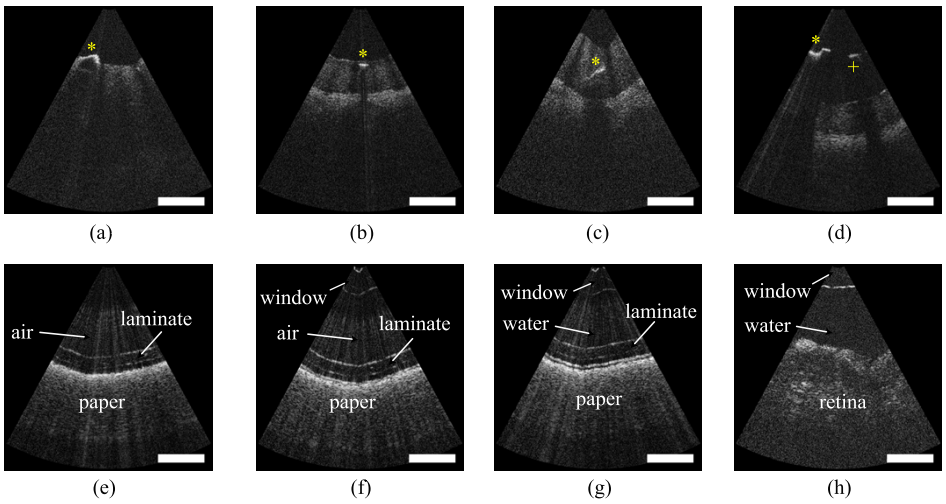


Fig. 7. (a-d) Imaging a needle relative to *ex vivo* retina; (e-h) effect of imaging through a glass window. (a) Needle, marked with '*', just above retinal tissue. (b) Needle penetrating into tissue. (c) Needle deeper in the tissue. (d) Needle above tissue, casting two shadows, that due to the needle close to the apex larger. Part of the needle is on the right-hand side of the image, indicated by a '+'. (e) Image of a laminated sheet of paper (for comparison). (f) The same sheet imaged through the thin glass window. (g) The same as (f) except water is present between the window and laminated paper. (h) Retinal tissue in water imaged through the window. The scale bars are 500 µm in air.

a miniaturized window reduce the usable working distance, rather it would make it safer for the probe to more closely approach the retina without the risk of damage.

4. Conclusions

We have demonstrated a forward-viewing OCT fiber endoscope which fits inside a protective outer tube with an inner diameter of 0.16 mm, resulting in an endoscopic probe with an outer diameter of just 0.31 mm. This is one of the smallest forward-viewing OCT probes reported to date, and is similar in size to the smallest reported side-viewing probes. Proximal rotation of the fiber probe allows a frame rate of at least 10 Hz with minimal apparent rotational distortion. While slower than conventional OCT scanners, this compares favorably with similar-sized ultra-miniature OCT probes, such as 0.5 Hz [17], 5 Hz [22] and 10 Hz [21]. A potential application in vitreoretinal surgery was demonstrated through *ex vivo* imaging of porcine retina and by real-time monitoring of a needle interacting with the retinal tissue.

While the prototype is fully functional, for most applications the outer tubing would also need to be sealed with an optically transparent window, both to prevent fouling of the fiber and to maintain an air interface distal to the angle-cleaved tip of the fiber. Including a miniaturized window would require additional engineering work, but we demonstrated that imaging through an oversized glass window is feasible in principle.

The lateral resolution of 16 µm at focus in the plane of the B-scan is within the typical range for endoscopic OCT systems and particularly with other ultraminiature systems (e.g. 10 µm [17]). Out-of-plane, the resolution is 25 µm due to the eccentricity of the focal spot. The usable imaging range of up to 2 mm is relatively short and could be extended by redesigning the distal focusing assembly, but at the cost of lateral resolution. This is a short working distance and is small compared with conventional OCT systems, but is shared with other devices which use

Biomedical Optics EXPRESS

GRIN fiber or narrow diameter GRIN lenses as a focusing element (e.g. [17,21,22]). The image circle circumference is 950 µm at a distance of 1 mm from the fiber tip. While this is small compared with side-viewing probes, it is a limitation shared with many forward-viewing OCT endoscopes. In principle, the image lateral size could be increased by increasing the beam exit angle, although this would also tend to increase beam eccentricity and impact resolution. The angle of the incident beam on the tissue is at 9° to the optical axis of the probe; while this would reduce signal from highly specular surfaces placed exactly perpendicular to the probe, for scattering tissue imaging applications, good signal is obtained.

The experiments reported here focused on demonstrating a proof-of-concept, where the tip of the probe was inside a rigid tube, and the remainder of the probe's length was not subject to significant bending. While this is a viable configuration for ophthalmic surgery, further work will be needed to assess the viability of the approach when more significant bending occurs, particularly with a small radius of curvature. This would include assessing both the mechanical integrity and any required correction of non-uniform rotational distortion (NURD) [34].

Funding. National Institute for Health and Care Research (NIHR202879, NIHR506200); Biomedical Research Center at Moorfields Eye Hospital NHS FT and UCL Institute of Ophthalmology (BRC4-05-RB413-302, BRC4-05-RB403-317); Medical Research Council (MRCIAA-MRC, MR/X502753/1); Engineering and Physical Sciences Research Council (EPSRC, EP/X000125/1); Royal Society (RG\R2\232087); Research Foundation - Flanders (G038925N).

Acknowledgments. This work was funded by the National Institute of Health and Care Research (NIHR) Invention for Innovation Programme NIHR202879, and NIHR506200. The views expressed are those of the authors and not necessarily those of the NIHR or the Department of Health and Social Care. Adrian Podoleanu acknowledges the Biomedical Research Centre at Moorfields Eye Hospital NHS FT and UCL Institute of Ophthalmology, BRC4-05-RB413-302 and BRC4-05-RB403-317, Imaging, Visual Assessment & Digital Innovation. Adrian Podoleanu and Michael Hughes also acknowledge Engineering and Physical Sciences Research Council, EPSRC, EP/X000125/1. Manuel Marques acknowledges the Royal Society Research Grant RG\R2\232087 and Fonds voor Wetenschappelijk Onderzoek, Research Foundation – Flanders, G038925N.

Disclosures. Adrian Podoleanu, Michael Hughes, Manuel Marques, and Radu-Florin Stancu are co-inventors on patents in the name of the University of Kent. Prof. Christos Bergeles holds shares and is on the Scientific Advisory Board of Conceivable Life Sciences.

Data availability. Data underlying the results presented in this paper are not publicly available at this time but may be obtained from the authors upon reasonable request.

References

1. M. J. Gora, M. J. Suter, G. J. Tearney, *et al.*, "Endoscopic optical coherence tomography: technologies and clinical applications [Invited]," Biomed. Opt. Express **8**(5), 2405–2444 (2017).
2. U. Sharma and J. U. Kang, "Common-path optical coherence tomography with side-viewing bare fiber probe for endoscopic optical coherence tomography," Rev. Sci. Instrum. **78**(11), 113102 (2007).
3. C. Duan, Q. Tanguy, A. Pozzi, *et al.*, "Optical coherence tomography endoscopic probe based on a tilted MEMS mirror," Biomed. Opt. Express **7**(9), 3345–3354 (2016).
4. T. Wu, R. Pan, K. Cao, *et al.*, "Side-viewing endoscopic imaging probe for swept source optical coherence tomography," Opt. Commun. **467**(2020), 125596 (2020).
5. T.-H. Tsai, B. Potsaid, Y. K. Tao, *et al.*, "Ultrahigh speed endoscopic optical coherence tomography using micromotor imaging catheter and VCSEL technology," Biomed. Opt. Express **4**(7), 1119–1132 (2013).
6. J. Li, S. Thiele, B. C. Quirk, *et al.*, "Ultrathin monolithic 3D printed optical coherence tomography endoscopy for preclinical and clinical use," Light: Sci. Appl. **9**(1), 124 (2020).
7. B. Paulson, S. Lee, Y. Kim, *et al.*, "Miniaturized omnidirectional flexible side-view endoscope for rapid monitoring of thin tubular biostructures," Biomed. Opt. Express **10**(5), 2264–2274 (2019).
8. D. O. Otuya, N. M. Dechene, D. Poshtupaka, *et al.*, "Passively scanned, single-fiber optical coherence tomography probes for gastrointestinal devices," Lasers Surg. Med. **54**(7), 935–944 (2022).
9. S. M. H. Jayhooni, G. Hohert, B. Assadsangabi, *et al.*, "A Side-Viewing Endoscopic Probe with Distal Micro Rotary Scanner for Multimodal Luminal Imaging and Analysis," J. Microelectromech. Syst. **30**(3), 433–441 (2021).
10. R. Volleberg, J.-Q. Mol, D. van der Heijden, *et al.*, "Optical coherence tomography and coronary revascularization: from indication to procedural optimization," Trends Cardiovasc. Med. **33**(2), 92–106 (2023).
11. E. Jelly, Z. A. Steelman, H. Zhang, *et al.*, "Next-generation endoscopic probe for detection of esophageal dysplasia using combined OCT and angle-resolved low-coherence interferometry," Biomed. Opt. Express **15**(3), 1943–1958 (2024).
12. J. Hu, S. Wu, G. Shi, *et al.*, "Design of an endoscopic OCT probe based on piezoelectric tube with quartered outside electrodes," Front. Bioeng. Biotechnol. **12**, 1391630 (2024).

Biomedical Optics EXPRESS

13. H.-C. Park, X. Zhang, W. Yuan, *et al.*, "Ultralow-voltage electrothermal MEMS based fiber-optic scanning probe for forward-viewing endoscopic OCT," Opt. Lett. **44**(9), 2232–2235 (2019).
14. L. M. Wurster, L. Ginner, A. Kumar, *et al.*, "Endoscopic optical coherence tomography with a flexible fiber bundle," J. Biomed. Opt. **23**(06), 1–8 (2018).
15. C. P. Fleming, H. Wang, K. J. Quan, *et al.*, "Real-time monitoring of cardiac radio-frequency ablation lesion formation using an optical coherence tomography forward-imaging catheter," J. Biomed. Opt. **15**(03), 1–3 (2010).
16. C. Schwarze, "A new look at Risley prisms," Photonics Spectra **40**(6), 67–71 (2006).
17. S. Han, M. V. Sarunic, J. Wu, *et al.*, "Handheld forward-imaging needle endoscope for ophthalmic optical coherence tomography inspection," J. Biomed. Opt. **13**(02), 1–3 (2008).
18. H. F. Fine, R. Iranmanesh, D. Iturralde, *et al.*, "Outcomes of 77 Consecutive Cases of 23-Gauge Transconjunctival Vitrectomy Surgery for Posterior Segment Disease," Ophthalmology **114**(6), 1197–1200.e3 (2007).
19. A. Savastano, C. Lenzetti, L. Finocchio, *et al.*, "Combining cataract surgery with 25-gauge high-speed pars plana vitrectomy: A prospective study," European Journal of Ophthalmology **31**(2), 673–678 (2021).
20. Y. Oshima, T. Wakabayashi, T. Sato, *et al.*, "A 27–Gauge Instrument System for Transconjunctival Sutureless Microincision Vitrectomy Surgery," Ophthalmology **117**(1), 93–102.e2 (2010).
21. X. Fu, D. Patel, H. Zhu, *et al.*, "Miniature forward-viewing common-path OCT probe for imaging the renal pelvis," Biomed. Opt. Express **6**(4), 1164–1171 (2015).
22. K. M. Joos and J.-H. Shen, "Miniature real-time intraoperative forward-imaging optical coherence tomography probe," Biomed. Opt. Express **4**(8), 1342–1350 (2013).
23. C.-P. Liang, J. Wierwille, T. Moreira, *et al.*, "A forward-imaging needle-type OCT probe for image guided stereotactic procedures," Opt. Express **19**(27), 26283–26294 (2011).
24. K. Broniarek and K. Michalska-Małecka, "Minimally Invasive Vitreoretinal Surgery (25G, 27G) with High-speed Vitrectomy Cutter – Case Series," Ophthalmology **27**(1), 50–53 (2024).
25. J. Li, S. C. Warren-Smith, R. A. McLaughlin, *et al.*, "Single-fiber probes for combined sensing and imaging in biological tissue: recent developments and prospects," Biomed. Opt. Express **15**(4), 2392–2405 (2024).
26. L. D. Cruz, K. Fynes, O. Georgiadis, *et al.*, "Phase 1 clinical study of an embryonic stem cell–derived retinal pigment epithelium patch in age-related macular degeneration," Nat. Biotechnol. **36**(4), 328–337 (2018).
27. E. Z. Ahronovich, N. Simaan, and K. M. Joos, "A Review of Robotic and OCT-Aided Systems for Vitreoretinal Surgery," Advances in Therapy **38**(5), 2114–2129 (2021).
28. A. J. Thirunavukarasu, M. L. Hu, W. P. Foster, *et al.*, "Robot-Assisted Eye Surgery: A Systematic Review of Effectiveness, Safety, and Practicality in Clinical Settings," Trans. Vis. Sci. Tech. **13**(6), 20 (2024).
29. C. S. Langlo, A. Amin, and S. S. Park, "Optical coherence tomography retinal imaging: narrative review of technological advancements and clinical applications," Annals of Translational Medicine **13**(2), 17 (2025).
30. Y. Qiu, Y. Wang, K. D. Belfield, *et al.*, "Ultrathin lensed fiber-optic probe for optical coherence tomography," Biomed. Opt. Express **7**(6), 2154–2162 (2016).
31. S. Balakrishnan and A. L. Oldenburg, "All-fiber probes for endoscopic optical coherence tomography of the large airways," Appl. Opt. **60**(22), 6385–6392 (2021).
32. C. Wang, X. Xia, S. Bia, *et al.*, "A numerical method for designing gradient-index fiber probes," *Proc. SPIE 8769, International Conference on Optics in Precision Engineering and Nanotechnology* 87693B (2013).
33. R.-F. Stancu, M. Hughes, T. Sanderson, *et al.*, "Fabrication and testing of lensed fiber-optic probes for distance sensing using common-path low-coherence interferometry," Appl. Opt. **64**(20), 5748–5753 (2025).
34. H. Zhang, J. Yang, J. Zhang, *et al.*, "Real-time correction of nonuniform rotational distortion in endoscopic OCT," *Proc. SPIE 12830, Optical Coherence Tomography and Coherence Domain Optical Methods in Biomedicine XXVIII*, 128300A (2024).